

Equations of state for B2 and bcc Fe_{1-x}Si_x

Yoshihiro Nagaya¹, Hitoshi Gomi², Kenji Ohta¹, and Kei Hirose¹

¹Tokyo Institute of Technology

²Earth-Life Science Institute

January 17, 2023

Abstract

Composition, chemical disorder, and magnetism significantly affect the volume and bulk modulus of iron–silicon (Fe–Si) alloys at ambient pressure. Here, we computed the equations of state for bcc-like (ordered B2 and disordered bcc) Fe–Si alloys available up to the inner-core pressure using the first-principles Korringa–Kohn–Rostoker method. Ferromagnetic (FM) and nonmagnetic (NM) states over a wide composition range, from Fe to FeSi, were investigated. The results revealed that magnetism and chemical disorder increased the volume and decreased the bulk modulus even at high pressures. Comparing the results with the preliminary reference Earth model, we found that an unrealistically large temperature gradient is required if the inner core is composed of a bcc-like Fe–Si alloy.

Hosted file

952948_0_art_file_10590094_r31cyk.docx available at <https://authorea.com/users/573578/articles/617803-equations-of-state-for-b2-and-bcc-fe1-xsix>

Hosted file

952948_0_supp_10568878_rnj3b7.docx available at <https://authorea.com/users/573578/articles/617803-equations-of-state-for-b2-and-bcc-fe1-xsix>

1 **Equations of state for B2 and bcc $\text{Fe}_{1-x}\text{Si}_x$**

2 Yoshihiro Nagaya^{1,*}, Hitoshi Gomi^{2,3,*}, Kenji Ohta¹, and Kei Hirose^{2,3}

3 ¹Department of Earth and Planetary Sciences, Tokyo Institute of Technology, Tokyo, Japan

4 ²Department of Earth and Planetary Science, The University of Tokyo, Tokyo, Japan

5 ³Earth-Life Science Institute, Tokyo Institute of Technology, Tokyo, Japan

6 * Corresponding authors. E-mail addresses: nagaya.y.ab@m.titech.ac.jp, hitoshi.gomi@eps.s.u-
7 tokyo.ac.jp

8

9 **Abstract**

10 Composition, chemical disorder, and magnetism significantly affect the volume and
11 bulk modulus of iron–silicon (Fe–Si) alloys at ambient pressure. Here, we computed
12 the equations of state for bcc-like (ordered B2 and disordered bcc) Fe–Si alloys
13 available up to the inner-core pressure using the first-principles Korringa–Kohn–
14 Rostoker method. Ferromagnetic (FM) and nonmagnetic (NM) states over a wide
15 composition range, from Fe to FeSi, were investigated. The results revealed that
16 magnetism and chemical disorder increased the volume and decreased the bulk
17 modulus even at high pressures. Comparing the results with the preliminary reference
18 Earth model, we found that an unrealistically large temperature gradient is required if
19 the inner core is composed of a bcc-like Fe–Si alloy.

20 **Plain Language Summary**

21 The center of the Earth is composed of a massive iron sphere known as the inner core,
22 with a radius of 1221 km. This inner core is subjected to high pressure (>330 GPa) and
23 temperature (approximately 5000 K). Under these extreme conditions, the density and
24 sound-wave propagation speed are very different from those of the materials on Earth’s
25 surface. Key unsolved problems pertaining to the inner core are its chemical
26 composition and crystal structure. To resolve this issue, computer simulations were
27 performed to determine the density and sound speed of Fe–Si alloys under temperature
28 and pressure conditions corresponding to the inner core. We investigated various
29 parameters of Fe–Si alloys while maintaining a crystal structure similar to that of iron
30 under ambient conditions. These parameters included the iron-to-silicon ratio, strength
31 of the magnetism of iron atoms, and the degree of ordering of atomic positions. These
32 parameters affected the density and sound speed; however, we found that no
33 combination of the parameters satisfied the seismic observations throughout the inner
34 core. Therefore, the inner core may have a different crystal structure or contain
35 impurities other than silicon.

36 **Key Points:**

- 37 ● We conducted first-principles calculations to obtain the equations of state for B2
38 and body-centered-cubic Fe–Si alloys.

- 39 ● The presence of magnetism and chemical disorder increased the volume and
40 decreased the bulk modulus of the examined Fe–Si alloys.
- 41 ● Single-phase bcc-like $\text{Fe}_{1-x}\text{Si}_x$ cannot satisfy the seismic observation of the Earth’s
42 inner core.

43 **1. Introduction**

44 Earth’s inner core is thought to be composed of an iron alloy containing nickel and a
45 small percentage of light elements (Birch, 1952; Hirose et al., 2021). Silicon is one of
46 the most likely candidates for the hypothesized light elements. A large amount of
47 silicon may have been incorporated into core-forming metals, particularly under
48 reducing conditions, to form Fe–Si alloys (McDonough et al., 2003; Ricolleau et al.,
49 2011). Comparisons of the Mg/Si and Fe/Si ratios between Earth’s mantle and
50 chondrites also indicate a possibility of silicon enrichment in the core (Allegre et al.,
51 1995). If silicon is the major light element in the inner core, in addition to the
52 aforementioned geochemical constraints, the density and elastic wave velocity of Fe–
53 Si alloys should match seismic observations (Mao et al., 2012; Sakamaki et al., 2016;
54 Shibazaki et al., 2016).

55 The crystal structure strongly influences the density and elastic-wave velocity of
56 metals. Previous diamond anvil cell experiments have suggested that the stable
57 structure of pure iron is a hexagonal close-packed (hcp) structure under the
58 temperature and pressure conditions of the inner core (Tateno et al., 2010; Sakai et al.,
59 2011). However, previous first-principles studies proposed two conflicting crystal
60 structures: the hcp structure (Stixrude & Cohen, 1995), and the body-centered cubic
61 (bcc) structure (Niu et al., 2015; Belonoshko et al., 2017). Furthermore, the bcc
62 structure can be stabilized by adding small amounts of impurities to iron (Vočadlo et
63 al., 2003; Kádas et al., 2009). Silicon is a bcc-stabilizer as Fe–Si alloys adopt bcc and
64 bcc-like structures such as B2 (Fischer et al., 2013; Tateno et al., 2015; Ozawa et al.,
65 2016; Edmund et al., 2019, 2022; Ikuta et al., 2021; Fu et al., 2022). B2 FeSi is an
66 ordered phase; iron and silicon atoms occupy the (0 0 0) and (1/2 1/2 1/2) sites,
67 respectively (Figure S1a). In contrast, bcc Fe–Si is a disordered phase in which the two
68 atoms are randomly aligned (Figure S1b). In this study, we focused on bcc and B2 $\text{Fe}_{1-x}\text{Si}_x$.

69 $_{x}\text{Si}_x$.

70 In addition to crystal structure, magnetism also affects the density and elastic-wave
71 velocity. Several researchers have investigated the relationship between magnetism and
72 the physical properties of bcc-like (bcc, B2, and DO₃) $\text{Fe}_{1-x}\text{Si}_x$ at ambient pressures
73 (Elsukov et al., 1992; Kudrnovský et al., 1991; Kulikov et al., 2002). Elsukov et al.
74 (1992) performed Mössbauer measurements on disordered crystalline and amorphous
75 $\text{Fe}_{1-x}\text{Si}_x$ alloys with variable silicon concentrations. Kudrnovský et al. (1991)
76 performed first-principles calculations for DO₃ $\text{Fe}_{3+x}\text{Si}_{1-x}$ with partial disordering using
77 the linear muffin-tin orbital method combined with the coherent potential
78 approximation (CPA) with fixed lattice parameters. These two studies (Elsukov et al.,
79 1992; Kudrnovský et al., 1991) showed that the local magnetic moment of iron
80 increases as the number of nearest-neighbor (NN) iron atoms increases (Kulikov et al.,
81 2002). Kulikov et al. (2002) used the Korringa–Kohn–Rostoker (KKR) method in
82 combination with CPA to calculate bcc $\text{Fe}_{1-x}\text{Si}_x$ with varying lattice parameters. Their
83 results demonstrated that the magnetic moment decreases with increasing silicon
84 concentrations, which causes a decrease in volume and an increase in the bulk
85 modulus. In summary, the magnetic moment varies with the number of NN iron atoms,
86 which is determined by the composition and chemical disorder, resulting in a volume
87 increase and a decrease in the bulk modulus.

88 In this study, we computed the equations of state (EoS) for $\text{Fe}_{1-x}\text{Si}_x$ under pressure
89 conditions matching the Earth’s inner core based on the KKR-CPA method (with and
90 without considering magnetism), regardless of its thermodynamic stability. We
91 considered the bcc and B2 structures, which maximize and minimize the number of
92 NN iron atoms, respectively. Using the present EoS, we calculated the density and bulk
93 sound velocity of $\text{Fe}_{1-x}\text{Si}_x$ alloys and compared them with the inner-core observations
94 provided by the Preliminary Reference Earth Model (PREM) (Dziewonski &
95 Anderson, 1981).

96 **2. Methods**

97 We obtained the equations of state of the $\text{Fe}_{1-x}\text{Si}_x$ alloys ($x = 0, 0.1, 0.2, 0.3, 0.4$, and

98 0.5) based on static first-principles calculations. Figure S1a shows the crystal structure
 99 of fully ordered B2 FeSi ($x = 0.5$). Figure S1b shows the bcc FeSi, in which the
 100 number of NN iron atoms and the degree of disordering are maximized. For non-
 101 stoichiometric compositions ($0 < x < 0.5$), the structure with the highest degree of
 102 ordering was B2, and the lowest was bcc. In the fully ordered B2 structure, the Fe sites
 103 were completely occupied by iron atoms, whereas Si sites were occupied by both iron
 104 and silicon atoms. Figure S1c shows the most ordered structure of the B2 Fe_{0.6}Si_{0.4}. In
 105 this structure, iron atoms occupy all the (0 0 0) sites (Fe sites) and 20% of the (1/2 1/2
 106 1/2) sites (Si sites). On the other hand, Fe and Si sites were not distinguished; thus,
 107 iron and silicon atoms were randomly positioned in the bcc structure (Figures S1a, d).
 108 In this study, we considered the structures with the highest and lowest degrees of
 109 ordering among the B2 and bcc structures.

110 The Kohn–Sham equation (Kohn & Sham, 1965) was solved using the KKR method
 111 (Akai, 1989). We used the CPA to simulate chemical disorder. We considered the
 112 ferromagnetic (FM) and non-magnetic (NM) states, which can be obtained by spin-
 113 polarized and non-spin-polarized calculations. The volume range was 75–200 Bohr³
 114 (11.11–29.64 Å³). The Perdew–Burke–Ernzerhof (PBE) type of generalized gradient
 115 approximation (GGA) was used as the exchange–correlation functional (Perdew et al.,
 116 1996). We treated relativistic effects within the scalar relativistic approximation. We
 117 calculated the wavefunction up to $l = 2$, where l is the angular momentum quantum
 118 number. This method has been used for the FeH_x system, with results consistent with
 119 those of previous experiments (Gomi et al., 2018; Tagawa et al., 2022; Gomi & Hirose,
 120 2022). We used a simple cubic lattice for a computational cell containing two atoms for
 121 all calculations. A k -point mesh of $20 \times 20 \times 20$ was used, corresponding to 1771
 122 points in the irreducible Brillouin zone.

123 The total energy was fitted to the third-order Birch–Murnaghan equation of state:

$$124 \quad E(V) = \frac{9V_0K_{T,0}}{16} \left\{ \left[\left(\frac{V_0}{V} \right)^{\frac{2}{3}} - 1 \right]^3 K' + \left[\left(\frac{V_0}{V} \right)^{\frac{2}{3}} - 1 \right]^2 \left[6 - 4 \left(\frac{V_0}{V} \right)^{\frac{2}{3}} \right] \right\} + E_0 \quad (1)$$

125 where E is the total energy, V is the volume, K_T is the isothermal bulk modulus, and K'
 126 is the pressure derivative. The subscript ‘0’ refers to the value at zero pressure. In the

127 spin-polarized calculations, we fitted the volume range in which the local magnetic
128 moment of the iron atom in the Fe site exists. The pressure $P = -dE/dV$ and isothermal
129 bulk modulus $K_T = V(d^2E/dV^2)_T$ were obtained from the analytical derivative.

130 **3. Results**

131 Figure 1 shows the results of the present equations of state for $\text{Fe}_{1-x}\text{Si}_x$ compared with
132 those of previous experiments (Dewaele et al., 2006; Edmund et al., 2019; Sata et al.,
133 2010). The fitting parameters are summarized in Table S1-4. The magnetic moment
134 (M_0), volume (V_0), and isothermal bulk modulus ($K_{T,0}$) were plotted at ambient
135 pressure (Figure 2). The combination of the crystal structure (B2 and bcc) and
136 magnetism (FM and NM) significantly changed these quantities.

137 Figure 1a shows FM B2 $\text{Fe}_{1-x}\text{Si}_x$, which best explains the previous experiments
138 (Dewaele et al., 2006; Edmund et al., 2019; Sata et al., 2010) for the combination of
139 magnetism and crystal structure investigated in this study. The volume was largest for
140 pure iron and decreased with increasing silicon concentrations (Figure 2b). This
141 volume change is related to the bulk magnetic moment (Kulikov et al., 2002). The bulk
142 magnetic moment at 0 GPa decreases with increasing silicon concentrations and
143 becomes zero for FeSi (Figure 2a). This is consistent with previous Mössbauer
144 measurements (Elsukov et al., 1992) and first-principles calculations (Kudrnovský et
145 al., 1991; Kulikov et al., 2002).

146 Figure 1b compares the NM B2 $\text{Fe}_{1-x}\text{Si}_x$ with previous experiments. Except for FeSi (x
147 = 0.5), where spin-polarized calculations yielded NM results, the volume of NM was
148 smaller than those calculated in previous experiments (Dewaele et al., 2006; Edmund
149 et al., 2019). This indicates the importance of magnetism in the equations of state for
150 $\text{Fe}_{1-x}\text{Si}_x$.

151 Figure 1c illustrates FM bcc $\text{Fe}_{1-x}\text{Si}_x$. Pure iron was reproduced in a previous
152 experiment (Dewaele et al., 2006). However, the difference between the present
153 calculation and previous experiments (Edmund et al., 2019; Sata et al., 2010) increased
154 with increasing silicon concentrations. Ferromagnetic bcc $\text{Fe}_{1-x}\text{Si}_x$ also showed a
155 decreasing bulk magnetic moment with increasing silicon concentrations, similar to

156 FM B2. However, at the maximum silicon concentration of FeSi ($x = 0.5$), B2 FeSi
157 became NM, whereas bcc FeSi remained FM. This difference in the compositional
158 dependence of the magnetic moment between B2 and bcc is consistent with previous
159 studies at 1 bar (Khmelevska et al., 2006; Rinaldi et al., 2021). This behavior can be
160 understood within the model, which suggests that the magnetic moment is proportional
161 to the number of NN iron atoms (Elsukov et al., 1992; Kudrnovský et al., 1991); all
162 bonds in B2 FeSi are Fe-Si, whereas 25% of the bonds in bcc FeSi are Fe-Fe.

163 Figure 1d shows the volume of NM bcc $\text{Fe}_{1-x}\text{Si}_x$ as a function of the pressure. The iron
164 volume was underestimated because of the absence of magnetism. Interestingly, the
165 equation of state of NM bcc FeSi differs from that of NM B2 FeSi. In the above
166 discussion, the relationship between the chemical disorder and volume was interpreted
167 as the effect of magnetism. However, the NM bcc $\text{Fe}_{1-x}\text{Si}_x$ results suggest that chemical
168 disorder also affects the volume and bulk modulus.

169 **4. Discussion**

170 The volume and bulk modulus are crucial in the examination of bcc-like $\text{Fe}_{1-x}\text{Si}_x$ alloys
171 as a predominant mineral in the inner core based on comparing their densities and bulk
172 sound velocities with seismic observations. Our important findings are as follows: 1)
173 The magnetic moment depends on the number of NN iron atoms, which changes with
174 silicon concentration and chemical disorder; 2) The higher the magnetic moment, the
175 larger the volume, and the smaller the bulk modulus; 3) Without considering
176 magnetism, the bcc alloy has a larger volume and lower bulk modulus than the B2
177 alloy.

178 While these findings are consistent with those of previous studies at ambient pressure
179 (Elsukov et al., 1992; Kudrnovský et al., 1991; Kulikov et al., 2002), they are not
180 consistent with the earlier high-pressure/room-temperature experiments performed by
181 Edmund et al. (2018), which identified the $\text{Fe}_{1-x}\text{Si}_x$ samples with $x > 0.21$ to be in the
182 metastable bcc phase. In contrast, our calculations for bcc $\text{Fe}_{1-x}\text{Si}_x$ did not reproduce
183 their equations of state (Figures 1c and 1d). There are two possibilities that may
184 explain this discrepancy. First, Edmund et al. (2018) misidentified the B2 and DO_3

185 structures as bcc. Body-centered cubic phase identification was based on the absence
186 of the diffraction line, which is characteristic of the ordered phase. However, the
187 intensity of this characteristic B2 line was weak and difficult to observe. Another
188 possibility is that the present calculations overestimated the effects of FM. In general,
189 GGA tends to overestimate the volume and magnetic moment. Indeed, the magnetic
190 moment obtained in this study was higher than that reported in the literature (Figure
191 2a). Furthermore, at finite temperatures, the bulk magnetic moment decreases owing to
192 the spin fluctuations.

193 The finite temperature effect on the magnetic disorder in magnetic phases becomes
194 more critical at the high temperatures corresponding to the inner core. The same is true
195 for the chemical disorder in the B2 phase. It is highly challenging to optimize the
196 thermodynamic properties of the chemical and magnetic order parameters, which may
197 vary continuously at finite temperatures. Alternatively, this study considers four
198 different combinations of crystal structure (B2 or bcc) and magnetism (FM or NM) as
199 end components to discuss the inner-core density and bulk sound velocity.

200 **5. Implications**

201 Figure 3 shows the density and bulk sound velocity as functions of pressure at 0 K for
202 B2 and bcc $\text{Fe}_{1-x}\text{Si}_x$. For FM, we plotted data only within the pressure range where
203 spin-polarized calculations provided a finite magnetic moment at the Fe site. In the
204 case of pure iron, it is possible to have local magnetic moments up to the inner-core
205 pressures. For bcc $\text{Fe}_{1-x}\text{Si}_x$, the pressure range with finite magnetic moments became
206 narrower as the silicon concentration increased. However, this pressure range becomes
207 wider for B2 $\text{Fe}_{1-x}\text{Si}_x$ than for bcc. Ferromagnetic material has a lower density and
208 slower bulk sound velocity than NM. However, these differences were smaller at
209 higher pressures. For all calculations, with increasing silicon concentrations, the
210 density decreased, and the bulk sound velocity increased. This finding is consistent
211 with those of Hirao et al. (2004) and Fischer et al. (2014).

212 For $\text{Fe}_{1-x}\text{Si}_x$ to be the sole constituent of the inner core, its density and bulk sound
213 velocity must be consistent with the seismic observations. Ferromagnetic and NM iron

214 have higher densities and slower bulk sound velocities than PREM values (Dziewonski
 215 & Anderson, 1981) at the inner-core-boundary (ICB) pressure and 0 K (Figure 4a).
 216 Alloying silicon causes a decrease in density and an increase in bulk sound velocity. At
 217 0 K, both the density and bulk sound volume of NM $\text{Fe}_{1-x}\text{Si}_x$ do not match the PREM
 218 simultaneously at any silicon concentration. In contrast, FM bcc $\text{Fe}_{1-x}\text{Si}_x$ with $x \sim 0.15$
 219 is closely consistent with the PREM. If the inner-core temperature is 0 K, NM $\text{Fe}_{1-x}\text{Si}_x$
 220 is no longer a candidate for the inner core, whereas FM bcc $\text{Fe}_{0.85}\text{Si}_{0.15}$ is a strong
 221 candidate. However, the inner core is in a high-temperature state ($T \sim 5000$ K), which
 222 reduces the density and bulk sound velocity. Therefore, we need to examine the effects
 223 of temperature on NM $\text{Fe}_{1-x}\text{Si}_x$.

224 We calculated the Helmholtz energies of NM B2 and bcc $\text{Fe}_{1-x}\text{Si}_x$ under inner-core
 225 conditions following Gomi and Hirose (2022). The contributions of the electrons were
 226 determined based on the density of states (DOS) of the system. The lattice vibration
 227 terms were examined using a quasi-harmonic approximation with the Debye model. To
 228 obtain the Debye temperature, we assumed that the Poisson's ratio of $\text{Fe}_{1-x}\text{Si}_x$ was
 229 identical to the PREM value; note that this assumption is valid when the inner core
 230 consists of $\text{Fe}_{1-x}\text{Si}_x$. Under this assumption, the high-temperature density and bulk
 231 sound velocity of bcc-like NM $\text{Fe}_{1-x}\text{Si}_x$ at ICB pressure and $T = 0$ K and 5000 K are
 232 compared with those of PREM in Figure 4b. We found that NM B2 $\text{Fe}_{1-x}\text{Si}_x$ ($x = 0.074$)
 233 explained both the PREM density and bulk sound velocity at $T = 4820$ K. With such a
 234 low silicon concentration, the values for bcc were similar to those for B2 at any depth
 235 of the inner core. Figure 5 shows the variations in the silicon content and temperature
 236 for NM bcc-like $\text{Fe}_{1-x}\text{Si}_x$ to simultaneously satisfy the PREM density and bulk sound
 237 velocity as a function of the radial position inside the inner core. This indicates that
 238 large gradients in both silicon concentration and temperature are required. However, if
 239 this is the case, the temperature difference between the ICB and the center of the Earth
 240 is 2300 K. For thermal stratification, the temperature gradient must be smaller than the
 241 adiabatic temperature gradient. However, $\Delta T = 2300$ K is much greater than the
 242 temperature difference of ~ 200 K along the adiabatic temperature gradient (Figure 5b)
 243 that is expressed as $T(r) = T_{\text{ICB}}(\rho(r)/\rho_{\text{ICB}})^\gamma$, where r is radial position in the inner core,
 244 ρ is density, and $\gamma = 1.45$ is the Grüneisen parameter for B2 $\text{Fe}_{1-x}\text{Si}_x$ at ICB conditions

245 (Equation S17). Therefore, the thermal stratification required for the B2 Fe–Si alloy to
246 be the inner-core material is not feasible. The effect of magnetism is weaker at higher
247 temperatures and pressures toward the center of the inner core, which further increases
248 the temperature gradient required. Therefore, the bcc-like $\text{Fe}_{1-x}\text{Si}_x$ binary alloy did not
249 explain the seismic observations of the inner core. Indeed, the eutectic liquid
250 composition in the Fe–FeSi system was estimated to be Fe + 8 wt.% Si ($\text{Fe}_{0.85}\text{Si}_{0.15}$) at
251 330 GPa (Hasegawa et al., 2021), suggesting that B2 Fe–Si alloy contains silicon
252 volumes that exceed the eutectic composition (>15 at.% Si) under inner-core
253 conditions. Since only 3–7 at.% silicon is required to explain the inner-core seismic
254 observations (Figure 5b), Si-rich B2 Fe–Si cannot be the predominant constituent of
255 the inner core.

256 **Acknowledgments**

257 This work was supported by JSPS MEXT/KAKENHI Grants 20K22365 and
258 22K03754. We would like to thank Editage (www.editage.com) for English language
259 editing.

260 **Open Research**

261 Datasets for this research are found in Table S1, S2, S3, and S4 available online
262 (<https://doi.org/10.5281/zenodo.7483988>)

263 **References**

- 264 Akai, H. (1989). Fast Korringa-Kohn-Rostoker coherent potential approximation and
265 its application to FCC Ni-Fe systems. *Journal of Physics: Condensed Matter*,
266 1(43), 8045. <https://doi.org/10.1088/0953-8984/1/43/006>
- 267 Allegre, C. J., Poirier, J. P., Humler, E., & Hofmann, A. W. (1995). The chemical
268 composition of the Earth. *Earth and Planetary Science Letters*, 134(3-4), 515-526.
269 [https://doi.org/10.1016/0012-821X\(95\)00123-T](https://doi.org/10.1016/0012-821X(95)00123-T)
- 270 Belonoshko, A. B., Lukinov, T., Fu, J., Zhao, J., Davis, S., & Simak, S. I. (2017).
271 Stabilization of body-centred cubic iron under inner-core conditions. *Nature*
272 *Geoscience*, 10(4), 312-316. <https://doi.org/10.1038/ngeo2892>

273 Birch, F. (1952). Elasticity and constitution of the Earth's interior. *Journal of*
274 *Geophysical Research*, 57(2), 227-286. <https://doi.org/10.1029/JZ057i002p00227>

275 Dewaele, A., Loubeyre, P., Occelli, F., Mezouar, M., Dorogokupets, P. I., & Torrent,
276 M. (2006). Quasihydrostatic equation of state of iron above 2 Mbar. *Physical*
277 *Review Letters*, 97(21), 215504. <https://doi.org/10.1103/PhysRevLett.97.215504>

278 Dziewonski, A. M., & Anderson, D. L. (1981). Preliminary reference Earth model.
279 *Physics of the Earth and Planetary Interiors*, 25(4), 297-356.
280 [https://doi.org/10.1016/0031-9201\(81\)90046-7](https://doi.org/10.1016/0031-9201(81)90046-7)

281 Edmund, E., Antonangeli, D., Decremps, F., Morard, G., Ayrinhac, S., Gauthier, M.,
282 Boulard, E., Mezouar, M., Hanfland, M., & Guignot, N. (2019). Structure and
283 elasticity of cubic Fe-Si alloys at high pressures. *Physical Review B*, 100(13),
284 134105. <https://doi.org/10.1103/PhysRevB.100.134105>

285 Edmund, E., Morard, G., Baron, M. A., Rivoldini, A., Yokoo, S., Boccato, S., Hirose,
286 K., Pakhomova, A., & Antonangeli, D. (2022). The Fe-FeSi phase diagram at
287 Mercury's core conditions. *Nature Communications*, 13(1), 1-9.
288 <https://doi.org/10.1038/s41467-022-27991-9>

289 Elsukov, E. P., Konygin, G. N., Barinov, V. A., & Voronina, E. V. (1992). Local atomic
290 environment parameters and magnetic properties of disordered crystalline and
291 amorphous iron-silicon alloys. *Journal of Physics: Condensed Matter*, 4(37),
292 7597. <https://doi.org/10.1088/0953-8984/4/37/007>

293 Fischer, R. A., Campbell, A. J., Caracas, R., Reaman, D. M., Heinz, D. L., Dera, P., &
294 Prakapenka, V. B. (2014). Equations of state in the Fe-FeSi system at high
295 pressures and temperatures. *Journal of Geophysical Research: Solid*
296 *Earth*, 119(4), 2810-2827. <https://doi.org/10.1002/2013JB010898>

297 Fischer, R. A., Campbell, A. J., Reaman, D. M., Miller, N. A., Heinz, D. L., Dera, P., &
298 Prakapenka, V. B. (2013). Phase relations in the Fe-FeSi system at high pressures
299 and temperatures. *Earth and Planetary Science Letters*, 373, 54-64.
300 <https://doi.org/10.1016/j.epsl.2013.04.035>

301 Fu, S., Chariton, S., Prakapenka, V. B., Chizmeshya, A., & Shim, S. H. (2022). Stable
302 hexagonal ternary alloy phase in Fe-Si-H at 28.6–42.2 GPa and 3000 K. *Physical*
303 *Review B*, 105(10), 104111. <https://doi.org/10.1103/PhysRevB.105.104111>

304 Gomi, H., Fei, Y., & Yoshino, T. (2018). The effects of ferromagnetism and interstitial
305 hydrogen on the equation of states of hcp and dhcp FeH_x: Implications for the
306 Earth's inner core age. *American Mineralogist: Journal of Earth and Planetary*
307 *Materials*, 103(8), 1271-1281. <https://doi.org/10.2138/am-2018-6295>

308 Gomi, H., & Hirose, K., (in press). Magnetism and equation of states of fcc FeH_x at
309 high pressure. *American Mineralogist: Journal of Earth and Planetary Materials*,
310 <https://doi.org/10.2138/am-2022-8452>

311 Hasegawa, M., Hirose, K., Oka, K., & Ohishi, Y. (2021). Liquidus phase relations and
312 solid-liquid partitioning in the Fe-Si-C system under core pressures. *Geophysical*
313 *Research Letters*, 48(13), e2021GL092681.
314 <https://doi.org/10.1029/2021GL092681>

315 Hirao, N., Ohtani, E., Kondo, T., & Kikegawa, T. (2004). Equation of state of iron–
316 silicon alloys to megabar pressure. *Physics and Chemistry of Minerals*, 31(6),
317 329-336. <https://doi.org/10.1007/s00269-004-0387-x>

318 Hirose, K., Wood, B., & Vočadlo, L. (2021). Light elements in the Earth's
319 core. *Nature Reviews Earth & Environment*, 2(9), 645-658.
320 <https://doi.org/10.1038/s43017-021-00203-6>

321 Ikuta, D., Ohtani, E., & Hirao, N. (2021). Two-phase mixture of iron–nickel–silicon
322 alloys in the Earth's inner core. *Communications Earth & Environment*, 2(1), 1-
323 10. <https://doi.org/10.1038/s43247-021-00298-1>

324 Khmelevska, T., Khmelevskiy, S., Ruban, A. V., & Mohn, P. (2006). Magnetism and
325 origin of non-monotonous concentration dependence of the bulk modulus in Fe-
326 rich alloys with Si, Ge and Sn: a first-principles study. *Journal of Physics:*
327 *Condensed Matter*, 18(29), 6677. <https://doi.org/10.1088/0953-8984/18/29/009>

328 Kohn, W., & Sham, L. J. (1965). Self-consistent equations including exchange and
329 correlation effects. *Physical Review*, 140(4A), A1133.
330 <https://doi.org/10.1103/PhysRev.140.A1133>

331 Kudrnovský, J., Christensen, N. E., & Andersen, O. K. (1991). Electronic structures
332 and magnetic moments of Fe_{3+y}Si_{1-y} and Fe_{3-x}V_xSi alloys with DO₃-derived
333 structure. *Physical Review B*, 43(7), 5924.
334 <https://doi.org/10.1103/PhysRevB.43.5924>

335 Kulikov, N. I., Fristot, D., Hugel, J., & Postnikov, A. V. (2002). Interrelation between
336 structural ordering and magnetic properties in bcc Fe-Si alloys. *Physical Review*
337 *B*, 66(1), 014206. <https://doi.org/10.1103/PhysRevB.66.014206>

338 Kádas, K., Vitos, L., Johansson, B., & Ahuja, R. (2009). Stability of body-centered
339 cubic iron–magnesium alloys in the Earth's inner core. *Proceedings of the*
340 *National Academy of Sciences*, 106(37), 15560-15562.
341 <https://doi.org/10.1073/pnas.0904859106>

342 Mao, Z., Lin, J. F., Liu, J., Alatas, A., Gao, L., Zhao, J., & Mao, H. K. (2012). Sound
343 velocities of Fe and Fe-Si alloy in the Earth's core. *Proceedings of the National*

344 *Academy of Sciences, 109(26),* 10239-10244.
345 <https://doi.org/10.1073/pnas.1207086109>

346 McDonough, W. F. (2003). 2.15–Compositional model for the Earth’s core. *Treatise*
347 *on geochemistry, 2,* 547-568. <https://doi.org/10.1016/B0-08-043751-6/02015-6>

348 Niu, Z. W., Zeng, Z. Y., Cai, L. C., & Chen, X. R. (2015). Study of the thermodynamic
349 stability of iron at inner core from first-principles theory combined with lattice
350 dynamics. *Physics of the Earth and Planetary Interiors, 248,* 12-19.
351 <https://doi.org/10.1016/j.pepi.2015.09.002>

352 Ozawa, H., Hirose, K., Yonemitsu, K., & Ohishi, Y. (2016). High-pressure melting
353 experiments on Fe–Si alloys and implications for silicon as a light element in the
354 core. *Earth and Planetary Science Letters, 456,* 47-54.
355 <https://doi.org/10.1016/j.epsl.2016.08.042>

356 Perdew, J. P., Burke, K., & Ernzerhof, M. (1996). Generalized gradient approximation
357 made simple. *Physical Review Letters, 77(18),* 3865.
358 <https://doi.org/10.1063/1.472933>

359 Ricolleau, A., Fei, Y., Corgne, A., Siebert, J., & Badro, J. (2011). Oxygen and silicon
360 contents of Earth’s core from high pressure metal–silicate partitioning
361 experiments. *Earth and Planetary Science Letters, 310(3-4),* 409-421.
362 <https://doi.org/10.1016/j.epsl.2011.08.004>

363 Rinaldi, M., Mrovec, M., Fähnle, M., & Drautz, R. (2021). Determination of spin-wave
364 stiffness in the Fe-Si system using first-principles calculations. *Physical Review*
365 *B, 104(6),* 064413. <https://doi.org/10.1103/PhysRevB.104.064413>

366 Sakai, T., Ohtani, E., Hirao, N., & Ohishi, Y. (2011). Stability field of the hcp-
367 structure for Fe, Fe-Ni, and Fe-Ni-Si alloys up to 3 Mbar. *Geophysical Research*
368 *Letters, 38(9),* L09302. <https://doi.org/10.1029/2011GL047178>

369 Sakamaki, T., Ohtani, E., Fukui, H., Kamada, S., Takahashi, S., Sakairi, T., Takahata,
370 A., Sakai, T., Tsutsui, S., Ishikawa, D., Shiraishi, R., Seto, Y., Tsuchiya, T., &
371 Baron, A. Q. (2016). Constraints on Earth’s inner core composition inferred from
372 measurements of the sound velocity of hcp-iron in extreme conditions. *Science*
373 *Advances, 2(2),* e1500802. <https://doi.org/10.1126/sciadv.1500802>

374 Sata, N., Hirose, K., Shen, G., Nakajima, Y., Ohishi, Y., & Hirao, N. (2010).
375 Compression of FeSi, Fe₃C, Fe_{0.95}O, and FeS under the core pressures and
376 implication for light element in the Earth’s core. *Journal of Geophysical*
377 *Research: Solid Earth, 115(B9).* <https://doi.org/10.1029/2009JB006975>

378 Shibazaki, Y., Nishida, K., Higo, Y., Igarashi, M., Tahara, M., Sakamaki, T., Terasaki,
379 H., Shimoyama, Y., Kuwabara, S., Takubo, Y., & Ohtani, E. (2016).

380 Compressional and shear wave velocities for polycrystalline bcc-Fe up to 6.3 GPa
381 and 800 K. *American Mineralogist*, 101(5), 1150-1160.
382 <https://doi.org/10.2138/am-2016-5545>

383 Shyni, P. C., & Alagarsamy, P. (2014). Thermomagnetic properties of nanocrystalline
384 Fe–Si alloys with high Si content. *Physica B: Condensed Matter*, 448, 60-63
385 <https://doi.org/10.1016/j.physb.2014.02.032>

386 Stixrude, L., & Cohen, R. E. (1995). High-pressure elasticity of iron and anisotropy of
387 Earth's inner core. *Science*, 267(5206), 1972-1975.
388 <https://doi.org/10.1126/science.267.5206.1972>

389 Tagawa, S., Gomi, H., Hirose, K., & Ohishi, Y. (2022). High-temperature equation of
390 state of FeH: Implications for hydrogen in Earth's inner core. *Geophysical*
391 *Research Letters*, 49(5), e2021GL096260. <https://doi.org/10.1029/2021GL096260>

392 Tateno, S., Hirose, K., Ohishi, Y., & Tatsumi, Y. (2010). The structure of iron in
393 Earth's inner core. *Science*, 330(6002), 359-361.
394 <https://doi.org/10.1126/science.1194662>

395 Tateno, S., Kuwayama, Y., Hirose, K., & Ohishi, Y. (2015). The structure of Fe–Si
396 alloy in Earth's inner core. *Earth and Planetary Science Letters*, 418, 11-19.
397 <https://doi.org/10.1016/j.epsl.2015.02.008>

398 Vočadlo, L., Alfè, D., Gillan, M. J., Wood, I. G., Brodholt, J. P., & Price, G. D. (2003).
399 Possible thermal and chemical stabilization of body-centered-cubic iron in the
400 Earth's core. *Nature*, 424(6948), 536-539. <https://doi.org/10.1038/nature01829>

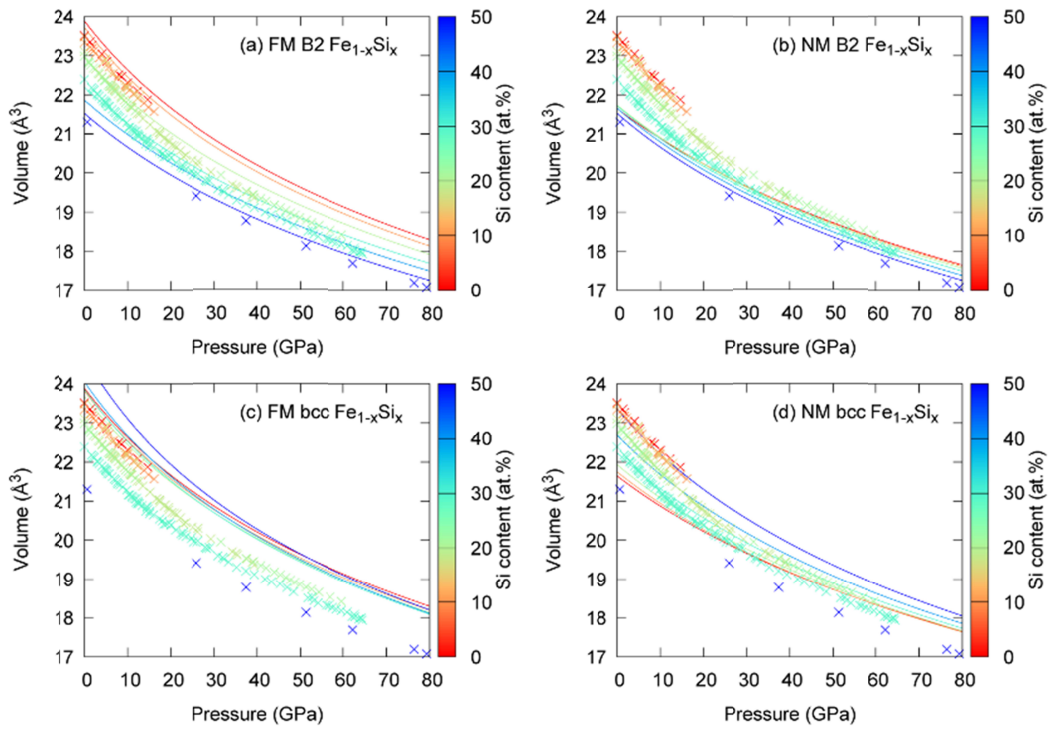
401 **References from the supporting information**

402 Blanco, M. A., Francisco, E., & Luana, V. (2004). GIBBS: isothermal-isobaric
403 thermodynamics of solids from energy curves using a quasi-harmonic Debye
404 model. *Computer Physics Communications*, 158(1), 57-72.
405 <https://doi.org/10.1016/j.comphy.2003.12.001>

406 Francisco, E., Recio, J. M., Blanco, M. A., Pendás, A. M., & Costales, A. (1998).
407 Quantum-mechanical study of thermodynamic and bonding properties of MgF₂.
408 *The Journal of Physical Chemistry A*, 102(9), 1595-1601.
409 <https://doi.org/10.1021/jp972516j>

410 Momma, K., & Izumi, F. (2011). VESTA 3 for three-dimensional visualization of
411 crystal, volumetric and morphology data. *Journal of applied crystallography*,
412 44(6), 1272-1276. <https://doi.org/10.1107/S0021889811038970>

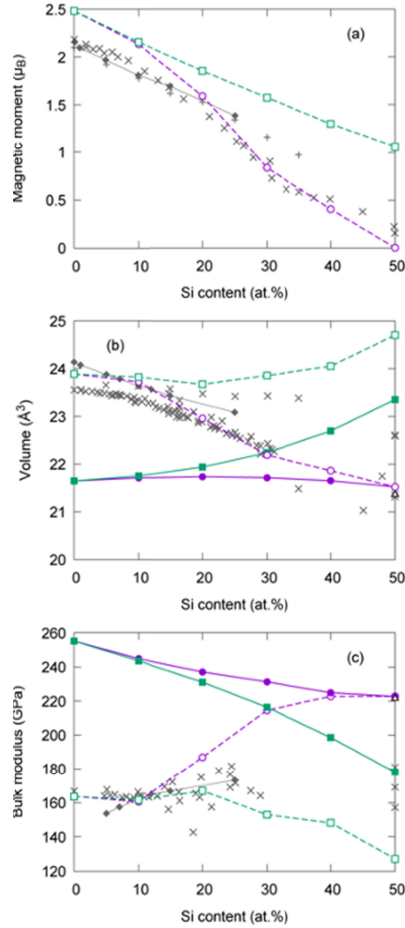
413 Moruzzi, V. L., Janak, J. F., & Schwarz, K. (1988). Calculated thermal properties of
414 metals. *Physical Review B*, 37(2), 790. <https://doi.org/10.1103/PhysRevB.37.790>



417

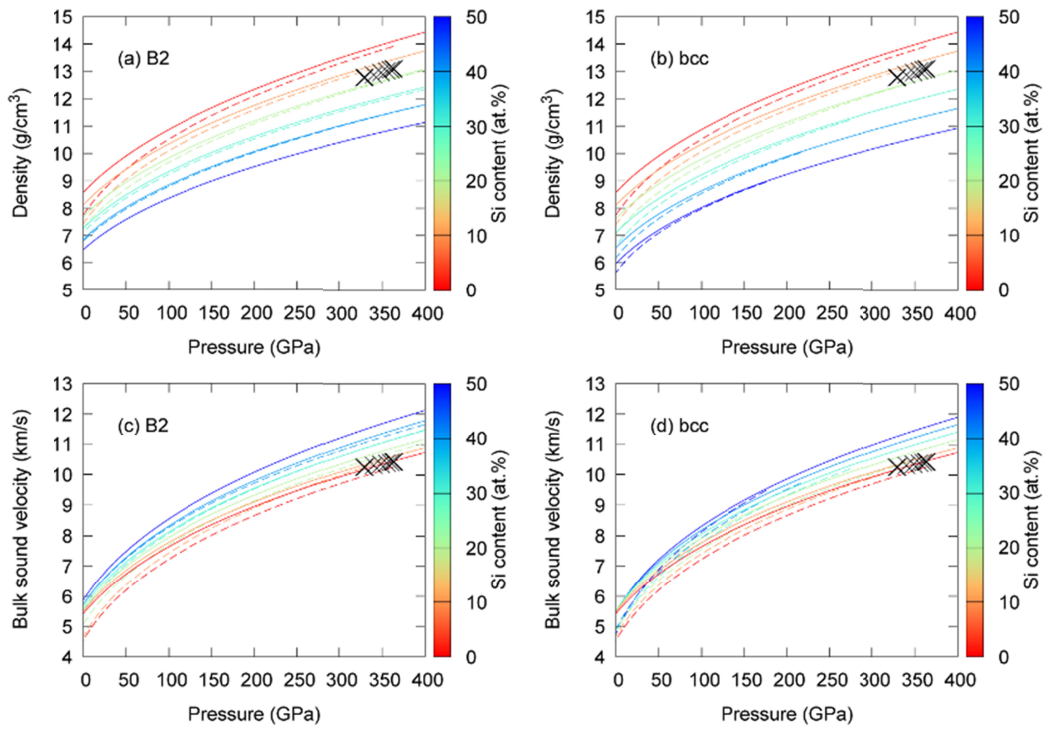
421 **Figure 1.** Present equations of state for: (a) ferromagnetic (FM) B2, (b) non-magnetic
 422 (NM) B2, (c) FM bcc, and (d) NM bcc Fe_{1-x}Si_x. The solid lines indicate the present
 423 calculations, and the cross symbols correspond to previous experiments for B2 and bcc
 424 Fe_{1-x}Si_x (Dewaele et al., 2006; Edmund et al., 2019; Sata et al., 2010).

422



423

432 **Figure 2.** (a) The bulk magnetic moment of ferromagnetic (FM) B2 (purple circles)
 433 and bcc (green squares) $\text{Fe}_{1-x}\text{Si}_x$ at 0 GPa. Earlier theoretical (\blacklozenge , Kulikov et al., 2002)
 434 and experimental (+, Shyni and Alagarsamy, 2014; \times , Elsukov et al., 1992 and
 435 references therein) studies are also plotted. (b) Ambient pressure volume of FM B2
 436 (open purple circles), non-magnetic (NM) B2 (filled purple circles), FM bcc (open
 437 green squares), and NM bcc (filled green squares) $\text{Fe}_{1-x}\text{Si}_x$. Previous theoretical (\blacklozenge ,
 438 Kulikov et al., 2002) and experimental (\triangle , Sata et al., 2010; \times , Edmund et al., 2019
 439 and references therein) data is shown for comparison. (c) Zero-pressure bulk modulus.
 440 The symbols are the same as those for the volume.



433

438 **Figure 3.** The density and bulk sound velocity as a function of pressure. Trends for B2

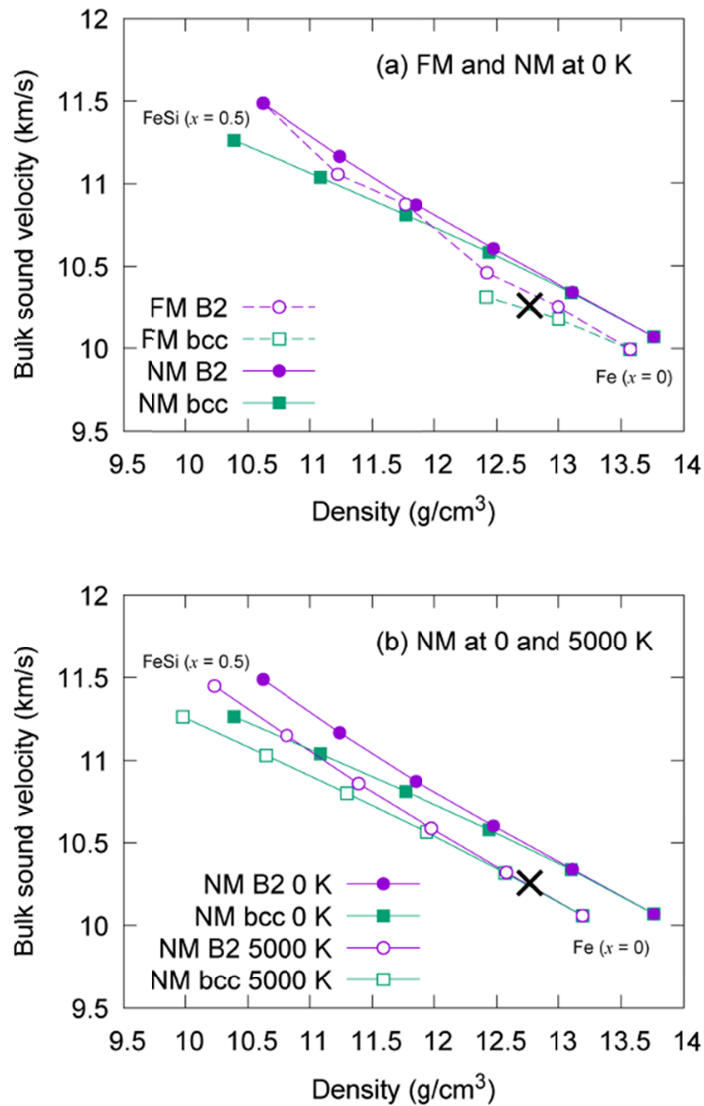
439 $\text{Fe}_{1-x}\text{Si}_x$ (a, c) and bcc $\text{Fe}_{1-x}\text{Si}_x$ (b, d) with $x = 0$ (red), 0.1, 0.2, 0.3, 0.4, and 0.5 (blue).

440 Solid and broken lines indicate ferromagnetic (FM) and non-magnetic (NM) states,

441 respectively. The cross symbols indicate the PREM values at the inner core

442 (Dziewonski and Anderson, 1981).

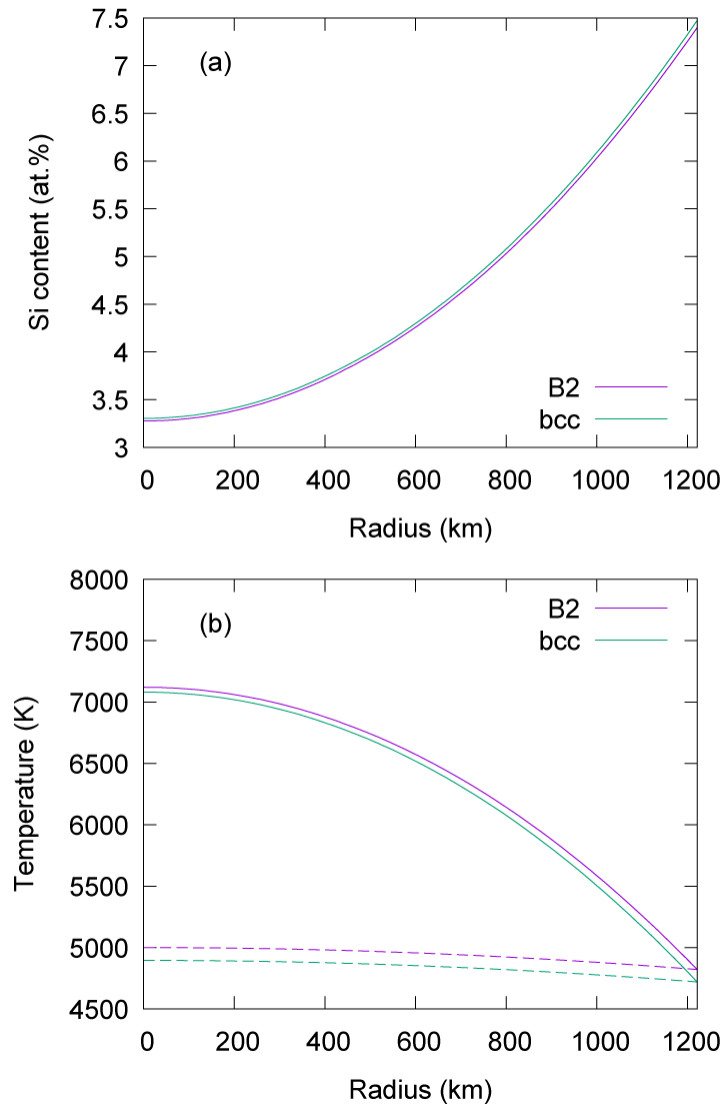
439



440

444 **Figure 4.** (a) The density and bulk sound velocity of B2 and bcc Fe_{1-x}Si_x alloys at the
 445 ICB pressure and 0 K. (b) The density and bulk sound velocity of B2 and bcc Fe_{1-x}Si_x
 446 alloys at the ICB pressure and both 0 and 5000 K; the PREM value is plotted as cross
 447 symbol for comparison (Dziewonski and Anderson, 1981).

445



445

446 **Figure 5.** (a) The Si content and (b) temperature profiles that simultaneously satisfy
 447 the density and bulk sound velocity of the PREM inner core (Dziewonski and
 448 Anderson, 1981). Note that the calculated temperature gradients (solid lines) are
 449 steeper than the adiabatic temperature gradients (broken lines), implying that bcc-like
 450 $\text{Fe}_{1-x}\text{Si}_x$ alone cannot explain the PREM (Dziewonski and Anderson, 1981).